Backscatter coefficient imaging using a clinical scanner

Evan J. Boote
Department of Radiology, University of Missouri, Columbia, Missouri 65212

James A. Zagzebski and Ernest L. Madsen
Department of Medical Physics, University of Wisconsin, Madison, Wisconsin 53706

(Received 13 September 1991; accepted for publication 21 May 1992)

A clinical ultrasound scanner has been integrated with a digital data acquisition system to record echo signals for off-line processing of quantitative acoustic backscatter images. The method used to determine backscatter coefficients accounts for experimental factors related to the beam directivity function, the transmitting and receiving electronics, and the attenuation path of the beam. After characterization and calibration of the ultrasound scanner according to the data processing requirements, the quantitative backscatter coefficient for tissue-mimicking phantoms are within 14% of a value predicted by scattering theory. On five normal volunteers, preliminary *in vivo* liver images of the acoustic backscatter coefficient are obtained. Results from this study are compared to previously published *in vitro* results.

I. INTRODUCTION

Current clinical ultrasound scanners provide images in which brightness levels are related to the amplitudes of backscattered echo signals from tissue. These images provide a qualitative impression of the scattering characteristics of the regions examined. However, due to complex factors which affect the amplitude and character of echo signals detected from the body, it is difficult to make quantitative assessments of scattering using these instruments. Thus, although many diffuse diseases, such as cirrhosis, are accompanied by changes in echogenicity,[1] current instruments do not allow precise diagnosis when subtle effects are present.

The parameter commonly used for quantifying ultrasonic scattering in tissues is the backscatter coefficient,[2] defined as the differential scattering cross section[3] per unit volume for a scattering angle of 180 deg. This quantity is an intrinsic property of the scattering medium and is believed to depend on changes in tissue structure and composition.[4] The backscatter coefficient is independent of the instrument, operator, and transmission path.

In previous papers, we described and presented results of quantitative tests of a method of data reduction for determining ultrasonic backscatter coefficients.[5-7] The method accounts for instrumental and propagation path dependencies on echo signal waveforms by closely modeling the production and detection of echo signals when a pulsed ultrasound transducer insonifies a medium containing randomly positioned scatterers. More recently, a laboratory system was used to construct quantitative ultrasound images, depicting the backscatter coefficient and relative backscatter contrast for a test object and excised tissues.[8,9]

The purpose of the work described in this paper was to adapt a clinical scanner to produce backscatter coefficient images. Results of tests in tissue mimicking phantoms and backscatter coefficients in liver of normal individuals are presented.

II. METHODS

A real-time mechanical sector scanner (Advanced Technology Laboratories, Mark III) was used (Fig. 1) in this study. The instrument is equipped with 3- and 5-MHz transducer assemblies, each consisting of three piezoelectric elements mounted 120° apart on a rotating wheel. The wheel is driven by a motor at 3 to 10 revolutions per s, permitting standard B-mode imaging at frame rates up to 30 Hz. B-mode images are formed from echo data acquired for up to 128 acoustic lines through arcs of 90 deg. or 45 deg. The system described in the following section is similar to one described by Meyer *et al.*[10]

For backscatter coefficient imaging, the transducer excitation and scan mechanism are identical to that used for *B*-mode imaging. However, echo data are recorded and processed off-line and images are formed in a computer. Echo signal acquisition is performed by fixing the transducer assembly to a 3-axis positioning device and then coupling to a test phantom or directly to a patient. Echo signals from the preamplifier stage of the scanner are digitized over 256 amplitude levels at 50 Megasamples per s using a LeCroy TR8828C transient recorder (Fig. 2). The transient recorder is housed in a CAMAC crate and is equipped with a 768 kbyte buffer memory. This unit is operated in "burst" mode, which allows efficient use of memory by storing data only when echo signals are present from a region of interest (ROI).

A "burst control" circuit was constructed to activate the transient recorder's storage mode when echo data from the region of interest are present. The burst control is triggered by scan and transmit pulse synchronization signals from the scanner. The user selects the ROI by setting a beginning and ending acoustic line from which data will be acquired and the starting and ending points of an acoustic line time gate. The storage of data in the transient recorder memory buffer is sequential and contains information only from within the region of interest. Data is transferred from the memory buffer to a Micro Vax computer via GPIB (IEEE-488) lines. Echo signals from multiple scanning

 0094-2405/92/51145-08$01.20

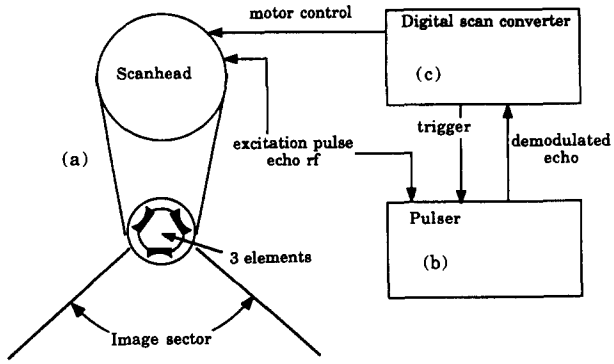

FIG. 1. Components of the ultrasound scanner used in this research (a) scan head with three ultrasound transducers on a rotating wheel (b) a pulser unit which sends the excitation pulse and receives the echo waveforms and (c) the digital scan converter, which forms the *B*-mode images from the amplitude data and also controls the motor turning the transducers.

planes are acquired by translating the scanhead 1 mm and repeating the acquisition process.

III. ANALYSIS

The analysis consists of calculating "backscatter estimators" from the echo voltage data and averaging these over a local volume to obtain backscatter values at locations in an image. The frequency domain scattered voltage signal from a volume centered at the point (l,m,n) is determined from

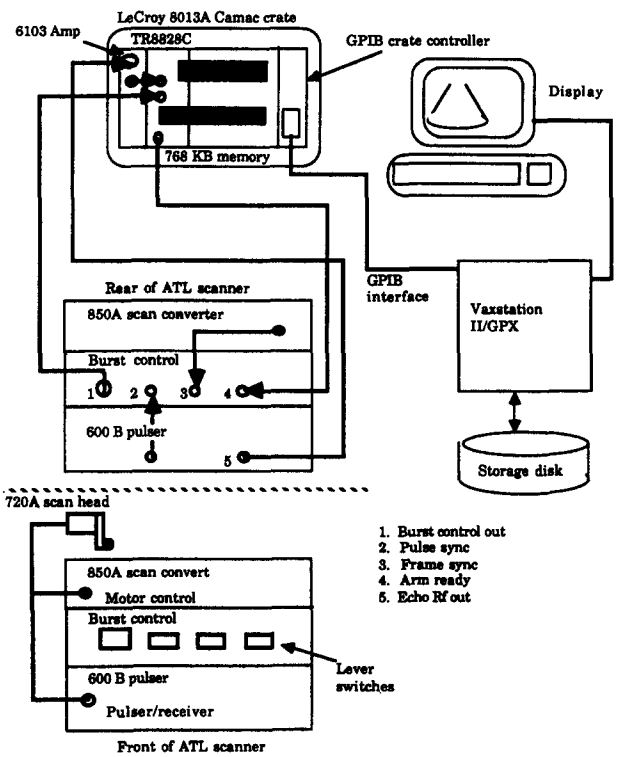

FIG. 2. Components used for digitizing echo rf waveforms from the clinical ultrasound scanner.

$$V_s(\omega_0,l,m,n)=\frac{1}{2\pi}\sum_{t=0}^{t=T_{\text{wave train}}}\Pi\left(\frac{t-l\tau}{\tau}\right)V_s'(t,m,n)e^{-i\omega_0 t}. \tag{1}$$

In Eq. (1), $\Pi(t-l\tau/\tau)$ is a rectangular gate of width τ applied to the rf wave train at a time represented by the index l, $V_s'(t,m,n)$ is the echo signal voltage at the transducer for a scan line at position (m,n), and m refers to the scan line number while n represents the scanning plane. Analysis of the echo signal is performed only at a singular frequency, denoted by ω_0.

Let $\eta_{l'm'n'}$ be the backscatter coefficient at analysis frequency ω_0 and pixel locations at depth l' and acoustic line m' in an image plane designated by n'. Then,

$$\eta_{l',m',n'}\cong\frac{1}{(\Delta L+1)(\Delta M+1)(\Delta N+1)}\times\sum_{l=l'-\frac{\Delta L}{2}}^{l'+\frac{\Delta L}{2}}\sum_{m=m'-\frac{\Delta M}{2}}^{m'+\frac{\Delta M}{2}}\sum_{n=n'-\frac{\Delta N}{2}}^{n'+\frac{\Delta N}{2}}\text{BSE}(\omega_0,l,m,n), \tag{2}$$

where $\text{BSE}(\omega_0,l,m,n)$ is a "backscatter estimator" and ΔL, ΔM, and ΔN are parameters which define the volume over which averaging of the backscatter estimators takes place. The backscatter estimator is calculated using

$$\text{BSE}(\omega_0,l,m,n)=|V_s(\omega_0,l,m,n)|^2/a_l(\omega_0), \tag{3}$$

where $V_s(\omega_0,l,m,n)$ is the Fourier transform as shown in Eq. (1). The denominator in Eq. (3) accounts for experimental factors which affect the amplitude of the echo signal. It is computed using

$$a_l(\omega_0)=\left(\frac{\tau}{2\pi}\right)^2\int\int\int_\Omega d\vec{r}\left|\int_{-\infty}^{+\infty}d\omega T(\omega)B_0(\omega)\times\frac{g(\omega)}{g(\omega_0)}\,\text{sinc}\left[\frac{(\omega-\omega_0)\tau}{2\pi}\right][A_0(\vec{r},\omega)]^2\right|^2, \tag{4}$$

where τ is the duration of the time gate used to select the lth segment of the signal; the sinc function is the representation of this temporal rectangular gate in frequency space; $T(\omega)$ and $B_0(\omega)$ represent the transducer–receiver "force-to-voltage transfer function" and the frequency content of the emitted acoustic pulse, respectively. The product $T(\omega)B_0(\omega)$ must then be determined experimentally, as shown in Sec. IV. The frequency-dependent backscatter coefficient is assumed to have the general form $\eta(\omega)=\eta_0[g(\omega)]^2$ where η_0 is a frequency-independent constant and $g(\omega)$ contains all the frequency dependence. When the frequency distribution of the interrogating ultrasound pulse is sufficiently symmetric about a center frequency, ω_0, it has been shown that setting $g(\omega)/g(\omega_0)=1$ does not change the computed $\eta(\omega_0)$ even when $g(\omega)$ is a strong function of ω.[9,11]

The volume integral in Eq. (4) includes all scatterers contributing to the signal segment as determined by the emitted pulse, the beam and the onset and termination of the time gate. The parameter $A_0(\vec{r},\omega)$ accounts for the beam shape of the transducer and is proportional to the

acoustic pressure at field point $\vec{r}$ and frequency ω. It is determined from the integral,

$$A_0(\vec{r},\omega_0)=\int\int_S ds\,\frac{e^{ik|\vec{r}-\vec{r}'|}}{|\vec{r}-\vec{r}'|}, \tag{5}$$

where S is the area of the transducer, $\vec{r}'$ ends on area element ds, and k is the complex wave number for the medium, given by

$$k=[\omega/c(\omega)]+i\alpha(\omega), \tag{6}$$

where $c(\omega)$ is the speed of sound and $\alpha(\omega)$ is the attenuation coefficient at frequency ω.

IV. CALIBRATIONS

Three experimental factors essential to accurately compute backscatter coefficients required measurement prior to or during the data collection process. These are (1) the size and shape of the radiating element, (2) the frequency response of the transducer and the corresponding force to voltage transfer function, and (3) the amplification applied to the time-domain rf signal just prior to digitization by the transient recorder.

A. Radiating element geometry

Individual transducers in the ATL scan head are identical single element focused disks. Computation of the quantity, $A_0(\vec{r},\omega)$ in Eq. (5) requires knowledge of the element diameter and radius of curvature. These were obtained by placing the scan head in a nonscanning mode, exciting the transducer with a narrow band burst with the beam propagating in distilled water and probing the beam with a 0.5-mm-diam. hydrophone. The hydrophone was scanned perpendicular to the beam axis, searching for the "radius of curvature" of the transducer element. This can be identified from beam plots because at the radius of curvature the resultant "lateral beam profile" is identical to the far field directivity function of an unfocused circular disk.[12] Thus the radius of curvature is taken as the axial distance to the plane in which the best fit to the far-field directivity pattern is obtained.

Figure 3(a) shows one such field plot for an element in the 5-MHz scan head. The radius of curvature was found to be 8.5 cm. The projected radius of the transducer was then obtained directly from the angular width of the directivity pattern and was determined to be 4.5 mm. The diameter and radius of curvature are used in Eq. (5) for computing $A_0(\vec{r},\omega)$.

Figure 3(b) shows a comparison between computed and measured lateral beam plots at a depth of 12 cm from this same transducer. One experimental plot is in the scan plane of the scan head, while the other is perpendicular to the scan plane. The in-plane profile is in excellent agreement with the profile computed using the geometric parameters determined in this experiment. Although the experimental profile perpendicular to the scan plane is in agreement with computations for most of the main lobe of the beam, the points far off axis are not. This is believed to be due to the shape of the window in the scan head, distorting the beam somewhat in the slice thickness direction. However, because most of the energy distributed in the beam is predicted by the beam model, these distortions were ignored in computing $A_0(\vec{r},\omega)$.

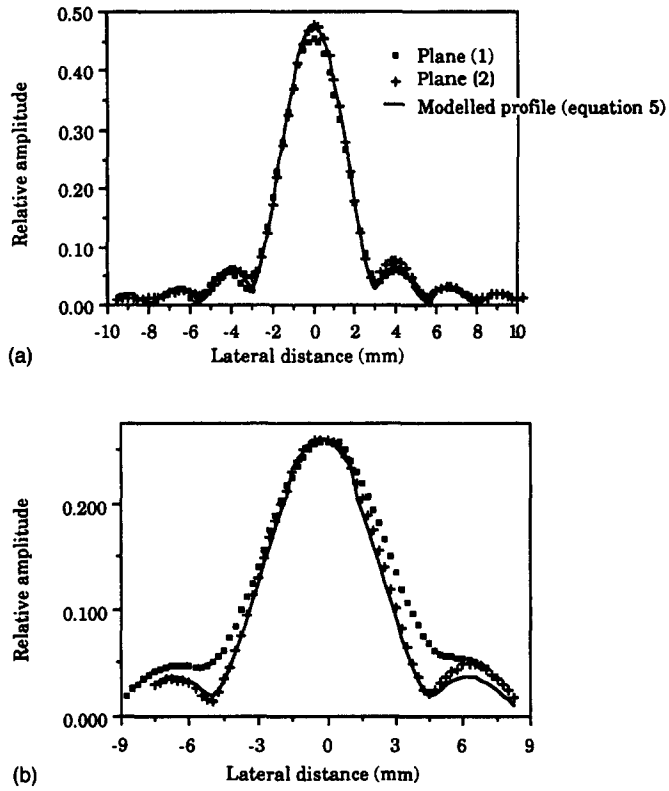

FIG. 3. (a) and (b) Lateral beam profiles of the 5 MHz ATL transducer assembly with transducer element No. 2 operating, compared with a lateral beam profile computed using the transducer model [Eq. (5) in the text]. (a) Lateral beam profile at 7-cm distance from the transducer and (b) lateral beam profile at 12-cm distance from the transducer.

B. Determination of $T(\omega)B_0(\omega)$

The relative efficiency of the transducer, it's frequency response and the sensitivity of the receiver are represented by the factors $T(\omega)B_0(\omega)$ in Eq. (3). $B_0(\omega)$ is used in the representation of the pulsed field from the ultrasound transducer, where the pressure pulse anywhere in the transducer field is represented as a superposition of continuous wave beams varying sinusoidally in time. $B_0(\omega)$ is a complex superposition coefficient in this representation.[13,14] The scattered wave from a point in the field integrated over the surface of the transducer produces a net force on the probe and $T(\omega)$ is the force-to-voltage transfer function for the system, in this case referred to the amplifier input. The product $T(\omega)B_0(\omega)$ can be obtained from the echo signal from a planar reflector[6] using

$$T(\omega)B_0(\omega)=V_r(\omega)\Big/R\int\int_{S_{\text{mirror}}} dSA_0(\vec{r},\omega), \tag{7}$$

where $V_r(\omega)$ is the Fourier transform of the echo signal, R is the amplitude reflection coefficient of the reflector and the integral $A_0(\vec{r},\omega)$ is over the surface of a mirror image

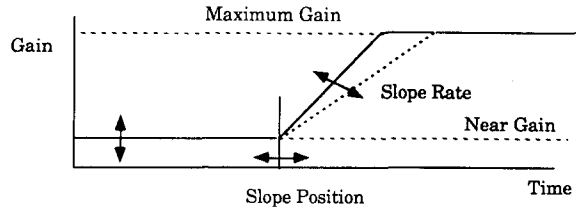

FIG. 4. Illustration of the components of the TGC controls for the ATL scanner. The near gain sets the initial gain and is constant throughout the entire span of time. The slope position sets the point at which a time-varying increase in gain begins. The slope rate sets the slope of this increase. The amplifiers have maximum possible gain which, once reached, will remain constant until the next sequence.

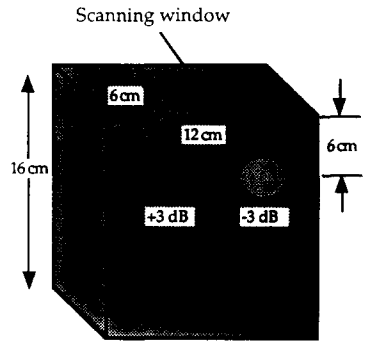

FIG. 5. Ultrasonically tissue-mimicking phantom used for testing. The phantom contains two 2-cm-diam. cylinders with scattering levels +3 dB and −3 dB with respect to the background material. 50-μm-thick Saran Wrap™ (Saran Wrap™ is a trademark of Dow Corning, Indianapolis, IN.) covers each end as acoustic scanning windows.

transducer at two times the transducer to reflector distance. Theoretically, the positioning of the planar reflector is independent of depth, since the beam profile is calculated. Experimental reproducibility of $T(\omega)B_0(\omega)$ is best when the planar reflector is positioned approximately in the focal plane of the transducer.[7,11]

To determine $T(\omega)B_0(\omega)$, the ATL probe was placed in a water tank above a planar reflector. The reflector was positioned approximately in the focal range of the transducer. With M-mode scanning activated, the transducer was aligned perpendicular to the planar reflector and the resulting echo signal $V_r(t)$ was digitized. $V_r(\omega)$ was determined for a set of frequencies using

$$V_r(\omega)=\frac{1}{2\pi}\sum_{t=0}^{t=T_{\text{pulse}}} V_r(t)e^{-i\omega t}. \tag{8}$$

This was then applied to Eq. (7) to compute $T(\omega)B_0(\omega)$ for a set of frequencies in the bandwidth of the pulse.

C. Time gain compensation

The digitized echo signal, $V_s(t,m,n)$, reflects the attenuation of the path of the ultrasonic beam. However, this signal already has a time gain compensation (TGC) applied prior to digitization. This is advantageous because it allows us to utilize the eight bit resolution of the transient recorder at all depths, but it requires that we calibrate these gain characteristics and apply a correction to obtain $V_s'(t,m,n)$, e.g., the echo signal voltage at the transducer.

The ATL scanner applies TGC in the preamplifier electronics. The scanner TGC has three user controlled functions (see Fig. 4): (1) an initial gain; (2) a slope delay and (3) a slope rate. Control settings were calibrated using an electronic phantom. This electronic phantom[15] provided a series of pulses separated in time by 2.5 μs, each pulse lasting approximately 2 cycles with a zero-crossing frequency of approximately 2.3 MHz. Pulses from the electronic phantom alternate between a positive voltage rise and a negative voltage rise to avoid a dc offset error. A $\times 10$ attenuator was placed in line between the electronic phantom and the pre-amplifier.

The initial gain, G_{near} was calibrated by comparing the input voltage from the electronic phantom to the output voltage from the preamplifier for each of the 10 settings of this control. The slope delay settings ($t_{\text{slope position}}$) were characterized with the same equipment. The initial gain was set to zero and the slope rate was set at its maximum value. From the signal trace on the oscilloscope, $t_{\text{slope position}}$, i.e., the time between the emission of the transmit pulse and the onset of an increasing slope in the amplification was determined. This was repeated for each setting of the slope position. The characterization of the slope rate was performed in a slightly different manner. In this case, the near gain and slope position were fixed, and the amplified signal was digitized and stored in the computer. The analysis of the signal involved determining the peak to peak voltage over narrow time windows for the entire length of the digitized waveform. The increase in amplification over time was converted to gain (in decibels) per μs. This was repeated for each potentiometer setting of the slope rate.

The time-dependent amplification of the ATL scanner, $G(t)$ is then computed according to the following rules:

$$G(t)=\begin{cases} G_{\text{near gain}}, & t\leqslant t_{\text{slope position}}, \\ G_{\text{near gain}}+(\text{slope rate})(t-t_{\text{slope position}}), & \\ t_{\text{slope position}}<t\leqslant t_{\text{maximum gain}}, & \\ G_{\text{maximum}}, & t>t_{\text{maximum gain}}, \end{cases} \tag{9}$$

where G_{maximum} is the maximum gain in the preamplifier. An example $G(t)$ is shown in Fig. 4. During digitization, the settings used on both the ATL scanner and the transient recorder amplifier/attenuator are recorded. $G_{\text{near gain}}$ is determined from the dB gain at the near gain setting. $t_{\text{slope position}}$ is taken from the time the amplification increase begins, dependent upon the slope position potentiometer setting as well as the slope rate. Following digitization and storage in the computer, the rf data are corrected for the gain applied using

$$V_s'(t,m,n)=[1/G(t)]V_s(t,m,n). \tag{10}$$

V. TESTS IN PHANTOMS

A. Methods

An ultrasonically tissue-mimicking phantom was used to test the accuracy of this quantitative imaging technique.

The phantom is diagrammed in Fig. 5. It was constructed using water-based gel,[16] with graphite powder (Superior 9039, Superior Graphite Co., Chicago) added to provide the desired attenuation and 59 micron mean diameter glass beads (Potters, type 2530) to provide ultrasonic scattering.[17,18] Two 2-cm-diam. cylindrical sections, one with 2 times the number density of glass beads as the background, the other with 1/2 this density, provide +3 dB and −3 dB backscatter contrast with respect to that of the main body of the phantom.

The attenuation and speed of sound of the TM material were measured using a narrow-band substitution technique[19] applied to test cylinders containing the material. Attenuation coefficients measured in the 1–7 MHz range were then fit to a function of the form $\alpha(f)=\alpha_1 f+\alpha_2 f^2$, where f is the frequency in MHz. For this phantom, $\alpha_1=0.480$ dB/cm/MHz and $\alpha_2=0.016$ dB/cm/MHz^2. The speed of sound in the material is 1538 m/s.

During data acquisition, the gain settings (overall gain, TGC, and damping) on the ATL scanner were optimized to utilize all 8 bits of digitization in the LeCroy transient recorder. Both probes available on the scanner (nominal frequencies of 3.5 and 5 MHz) were used in the study. Data was collected from 4 parallel planes in the phantom. The translational distance between planes was 1 mm. Once these data were stored in the computer, the transducer was mounted above a planar reflector and the echo voltage recorded. This echo signal was then used to determine $T(\omega)B_0(\omega)$ as discussed in Sec. IV B.

Echo signals from 128 scan lines per sector ×4 planes (=512 scan lines) were analyzed in the manner previously described. The duration of the segmental gates applied to the echo wavetrain was 3 μs. When the backscatter estimators are averaged together [as per Eq. (2)], a set of $\eta(\omega_0)_{l'm'n'}$ are obtained. A total of 64 backscatter estimators were used, e.g., a 4×4×4 "cube." Because of the sector scan format, the size of the volume used to determine each backscatter coefficient varies due to the distance between scan lines at the near axial depths versus the far axial depths. At a depth where the lateral distance between scan lines is 1 mm, the volume of the cube is 4×4×8 mm=128 mm^3.

B. Results

Figure 6(a) and (b) is backscatter coefficient and *B*-mode images at 2.75 MHz. Both the +3 dB and −3 dB scattering regions are easily distinguished from the background. Note in Figs. 6(a) that there is some specular reflection from the proximal and distal edges of these regions. There are also some echoes due to reverberations visible in the deeper portions of the phantom. (Note: The dark regions within the white bands of these reverberations are due to high "backscatter values." The image pixels are mapped to black when the maximum backscatter gray map value is exceeded.)

Table I presents numerical values for the backscatter coefficients determined from ROIs in the images. The backscatter coefficients in the background regions of the

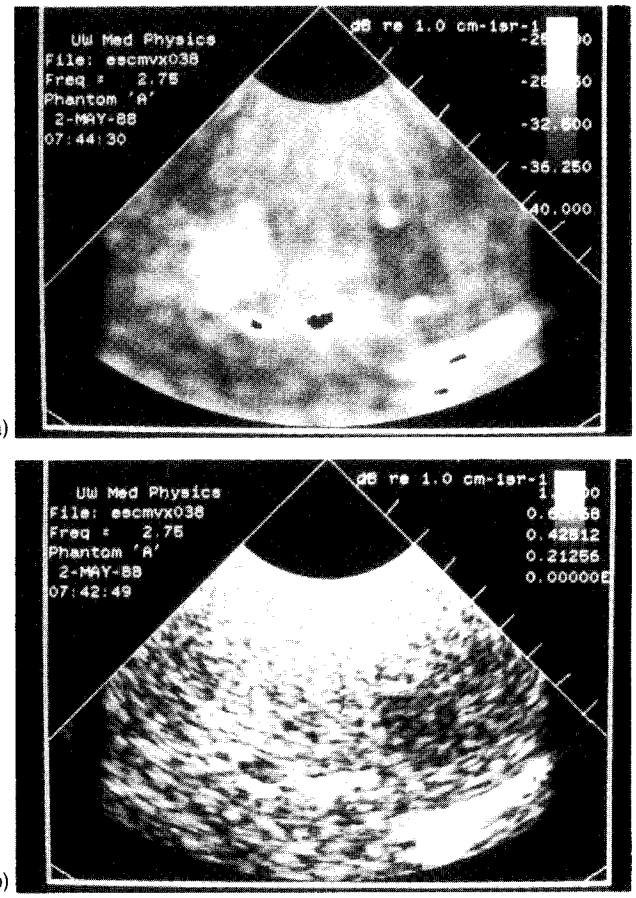

FIG. 6. (a) Backscatter coefficient image of the phantom using a frequency of 2.75 MHz. (b) *B*-mode image of the phantom constructed from data recorded using the digitizing system.

phantom are compared to predicted backscatter coefficients computed from characteristics of the phantom and the theory of Faran.[20] In each case, the experimental result is within 14% of the predicted value. Backscatter coefficients for cylindrical volumes within the phantom are determined with respect to the background. It can be seen, both in the images and in the quantitative results that the backscatter coefficients are properly portrayed.

VI. HUMAN STUDIES

A. Subjects

Preliminary *in vivo* backscatter coefficients were measured in five individuals. The subjects for this study were normal, healthy adult volunteers, four males and one female, between the ages of 24 and 27.

Before data were taken using the ATL system, the subjects were scanned using an Acuson Model 128 ultrasound scanner and Kitecko© (3M Co.) standoff pads. This was done in order to estimate the body wall thickness of each subject at the site where subsequent backscatter coefficient images would be obtained. A 5-MHz Acuson transducer (L538) was aimed in either a transverse or longitudinal direction below the rib cage approx 8 cm to the right of the midline. Measurements of the thickness of the subcutaneous fat layer and the abdominal muscles were made

TABLE I. Experimentally determined backscatter coefficients for phantom *A* using the ATL system [images in Figs. 6(a) and (b)] compared with predicted values calculated using expressions of Faran.[20]

Frequency ω_0 (MHz)	Backscatter coefficient of background ($cm^{-1}sr^{-1}$)		Backscatter coefficients in cylindrical volumes in dB relative to background	
	Predicted	Experiment	−3 dB	+3 dB
2.75	4.0×10^{-4}	4.55×10^{-4}	−2.8	+3.5
4.0	1.5×10^{-3}	1.73×10^{-3}	−2.6	+2.9

from the interfaces between each layer, using the calibrated cursors on the Acuson scanner. These thickness measurements were recorded for subsequent use in the backscatter coefficient image data analysis.

The subject was then scanned using the ATL system. Echo signals were recorded from the right anterior lobe of the liver through the same subcostal acoustic window from which the previous thickness measurements were made. Data were acquired from 4 parallel image sectors, each approximately 1 mm apart during a single breath hold by the subject. Data were analyzed in the same manner described previously, except the fat and muscle layers were accounted for in the effective wave number [Eq. (5)] (see Appendix). The speeds of sound and attenuation coefficients used were 1460 m s^{-1} and 0.6 dB cm^{-1} MHz^{-1} for fat; 1600 m s^{-1}, and 1.3 dB cm^{-1} MHz^{-1} for muscle.[21] The attenuation and speed of sound in normal liver were assumed to be 0.5 dB $cm^{-1}MHz^{-1}$ and 1570 m s^{-1}, respectively. These values were determined from a comprehensive review of published *in vivo* measurements from a variety of researchers.[22] The *in vivo* speed of sound is from a recent clinical study of 21 normal, healthy volunteers.[23]

B. Results from the *in vivo* study

Figure 7(a) is a backscatter coefficient image from one of the subjects. This is a longitudinal image of the liver; the right kidney is visible at the lower right of this image, the remaining part of the image is the right lobe of the liver. Figure 7(b) is the corresponding *B*-mode image for comparison. The backscatter coefficient image displays a rather uniform shade of gray over the liver, indicating a consistent backscatter coefficient. The attenuation estimate used in the data analysis seems reasonable considering the relatively uniform brightness with respect to depth. Larger vessels are visible on the backscatter coefficient image, even though it has been smoothed due to the averaging of backscatter estimators according to Eq. (2). These large vessel or organ interfaces should be avoided in any region of interest analysis, else artificially high backscatter coefficient results would be obtained.

Figure 8(a) is a backscatter coefficient image taken using the 5-MHz assembly. Figure 8(b) is the corresponding *B*-mode image. Because of the higher frequency, penetration into the liver is not as deep and, due to the signal losses from attenuation, electronic noise begins to dominate the signal from deeper regions. The electronic noise is manifested by the light gray band seen in the lower left portion of the image in Fig. 8(a).

Following each backscatter coefficient image formation, a region of interest analysis was performed on the liver parenchyma. The analysis was aimed at regions where a fairly uniform gray level was seen, with no significant infiltration of large reflecting surfaces. Table II is a summary of body wall thickness and backscatter coefficient measurements for the five subjects in this study. The overall mean backscatter coefficient at 2.75 MHz was 7.9×10^{-4} $cm^{-1}sr^{-1}$ with a standard deviation of 2.3×10^{-4} $cm^{-1}sr^{-1}$. At 4.0 MHz, the mean backscatter coefficient was 3.1×10^{-3} $cm^{-1}sr^{-1}$ with a standard deviation of 1.7×10^{-3} $cm^{-1}sr^{-1}$.

O'Donnell[24] has reported an average *in vivo* backscatter coefficient in six normal subjects of 3.5×10^{-4} $cm^{-1}sr^{-1}$ at 2.25 MHz. However, he used a different esti-

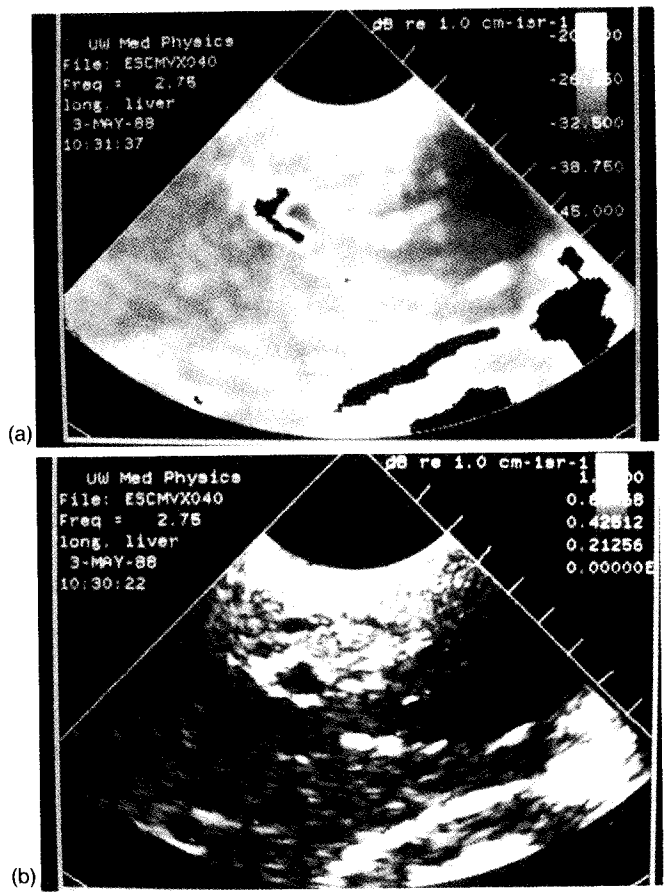

FIG. 7. (a) Backscatter coefficient image of one of the subjects at 2.75 MHz. (b) *B*-mode image of the subject for comparison with the backscatter coefficient image.

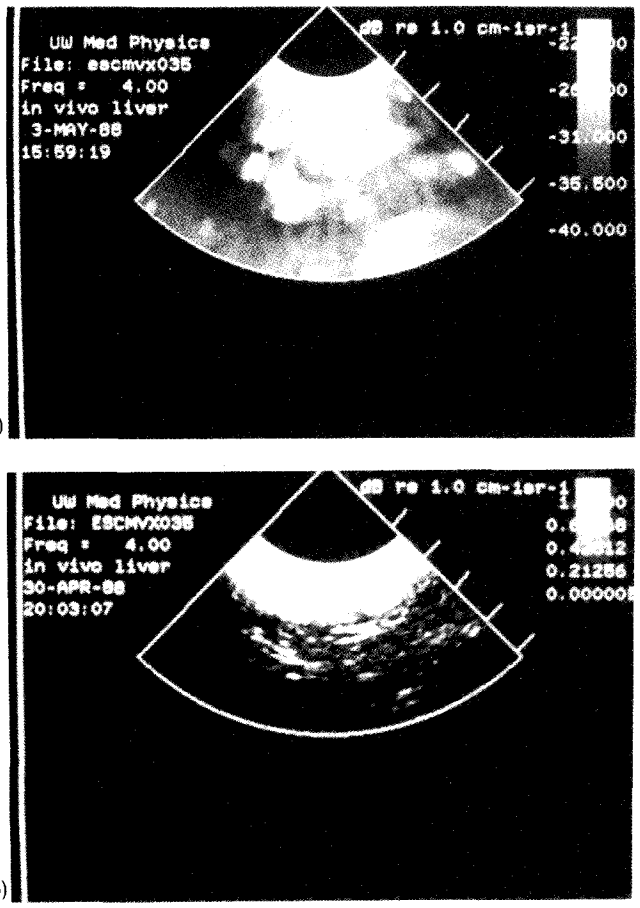

FIG. 8. (a) Backscatter coefficient image of one of the subjects using the 5-MHz probe. The analysis frequency is 4.0 MHz. (b) Corresponding *B*-mode image of the subject for comparison with the backscatter coefficient image.

mation for body wall losses and processed envelope detected signals from the scan converter of a clinical ultrasound imager. These results are reasonably similar when the frequency dependence of scattering is taken into account. A comparison to *in vitro* scattering measurements also has a reasonable level of agreement. The backscatter coefficient measured by our experiment at 2.75 MHz is 6% higher than that reported by Nicholas.[25] The value at 4 MHz from our study is approximately a factor of two greater than the value predicted by this previous report.

VII. SUMMARY AND DISCUSSION

In previous work, we reported on a method to produce images of the acoustic backscatter coefficient. This method explicitly accounts for experimental factors which affect the voltage signal resulting from echoes recorded from a volume of material. It has yielded accurate results for the backscatter coefficient in phantoms.

In this work, we have adapted a clinical ultrasound scanner to be used in conjunction with a transient recorder and a computer for generation of quantitative ultrasound images of the backscatter coefficient. Incorporation of a clinical ultrasound scanner poses more problems in terms of calibrations and equipment characterization than the laboratory system used in previous work. However, even with these difficulties, reasonable results were still obtained with the scanner using tissue-mimicking phantoms.

Apparent errors in the beam profile calculation (Sec. IV A) did not affect our measurements. This was because the depths from which echo signals were recorded were proximal to the focal plane of the transducer, whereas the disagreement between our model and measured beam profiles occurs beyond the focal plane of the element.

An additional set of variables are introduced when a human subject replaces the tissue-mimicking phantom, as described in Sec. VI. In this first attempt at quantification of the backscatter coefficient *in vivo*, we have tried to correct for overlying body wall layers by measurement of the wall thickness and by using approximations of the speed of sound and attenuation of these layers. However, other variables are present in this work as well, such as the attenuation of the tissue under investigation. For a relatively homogeneous organ, one could use an initial approximation, then estimate the attenuation using a previously proposed iterative technique.[8] The results are comparable to those reported earlier for an *in vitro* measurement. The larger error at 4 MHz could be due to electronic noise present in the echo signal as the gain is increased at this frequency. This error was not experienced in the phantom data (at the higher frequency) since the echo signals from the phantom were of greater amplitude due to a direct acoustic path. In the human data, the acoustic pulse was attenuated through fat and muscle layers. There is also the possibility that phase abberation due to the fat and muscle layers has affected these data. However, it is reasonable to

TABLE II. Summary of body wall thickness and backscatter coefficient measurements of liver from data in the human study.

	Body wall thickness (mm)		Backscatter coefficients from liver measured *in vivo* ($cm^{-1}sr^{-1}$)	
Subject No.	Fat	Muscle	2.75 MHz	4.0 MHz
1	4	9	7.2×10^{-4}	1.1×10^{-3}
2	7	12.5	5.7×10^{-4}	5.4×10^{-3}
3	4.5	14.5	9.6×10^{-4}	4.1×10^{-3}
4	7	13	1.1×10^{-3}	2.8×10^{-3}
5	4	11	6.0×10^{-4}	1.9×10^{-3}
Mean ± standard deviation			$7.9\pm2.3\times10^{-4}$	$3.1\pm1.7\times10^{-3}$

expect that phase abberation error would decrease rather than increase the estimate of backscatter coefficients.

We have shown that it is possible to characterize and calibrate a clinical ultrasound instrument to produce quantitative images. We have also reported preliminary acoustic backscatter coefficient measurements on human subjects *in vivo*. However, additional research is required to establish clinical accuracy and potential for diagnosis.

ACKNOWLEDGMENTS

The authors would like to thank Timothy Hall for his assistance in this work. This work was supported in part by Grants RO1CA39224 and RO1CA25634 from the National Institutes of Health.

APPENDIX

It has been shown that Eq. (4) can be used to model the beam profile of planar disk and focused transducers insonifying a "homogeneous" medium. However, in this experiment we acquired echo signals through several "inhomogeneous" layers. To compute the beam profile for this case we utilized an "effective wave number," K_{eff}, which was determined using an effective speed of sound $c(\omega)_{\text{eff}}$ and attenuation coefficient $\alpha(\omega)_{\text{eff}}$ in this transmission path. For example, at a given depth z,

$$c(w)_{\text{eff}}=\frac{1}{z}\left[c(w)_{\text{fat}}z_{\text{fat}}+c(w)_{\text{muscle}}z_{\text{muscle}} +c(w)_{\text{tissue}}(z-z_{\text{fat}}-z_{\text{muscle}})\right] \quad \text{(A1)}$$

$$\alpha(w)_{\text{eff}}=\frac{1}{z}\left[\alpha(w)_{\text{fat}}z_{\text{fat}}+\alpha(w)_{\text{muscle}}z_{\text{muscle}} +\alpha(w)_{\text{tissue}}(z-z_{\text{fat}}-z_{\text{muscle}})\right] \quad \text{(A2)}$$

In Eqs. (A1) and (A2), z_{fat} and z_{muscle} are the thickness of these layers in the body wall as estimated from ultrasound images and $c(\omega)_i$ and $a(\omega)_i$ are the speed of sound and attenuation coefficient of the *ith* component of the propagation path. Using these relationships and the measurements of the fat and muscle thicknesses on the subjects using the high resolution *B*-mode scanner, a first order approximation of the effects of overlying structures was made. Included in this approximation was the assumption that the fat and muscle layers were layered in parallel planes. Additionally, the measurement of layer thicknesses were made using the speed of sound for which the scanner is calibrated (1540 m/s). Using values of c and $\alpha(f)$ for fat and muscle in Sec. VI A, one can correct the measured thicknesses and then apply Eqs. (A1) and (A2) for the effective speed of sound and attenuation. These corrections are quite small and were not applied in our study. Using volunteer 4 (7 mm and 13 mm of fat and muscle, respectively) as an example, for an apparent depth (z) of 80 mm the effective speed of sound is calculated to be 1565.25 m/s and the effective attenuation is 0.639 dB/cm/MHz. When the corrections are applied, the speed of sound and attenuation coefficient are 1566.00 m/s and 0.641 dB/cm/MHz, respectively.

[1]B. B. Goldberg, *Abdominal Ultrasonography* (Wiley, New York, 1984), 2nd ed.
[2]R. A. Sigelmann and J. M. Reid, "Analysis and measurement of ultrasound from an ensemble of scatterers excited by sine-wave bursts," J. Acoust. Soc. Am. **53**, 1351–1355 (1973).
[3]P. M. Morse and H. Feshbach, *Methods of Theoretical Physics* (McGraw-Hill, New York, 1953).
[4]J. M. Reid, *Medical Physics of CT and Ultrasound: Tissue Imaging and Characterization*, edited by G. Fullerton and J. Zagzebski (AAPM Monograph No. 6, 1980), pp. 388–408.
[5]E. L. Madsen, M. F. Insana, and J. A. Zagzebski, "Method of data reduction for accurate determination of acoustic backscatter coefficients," J. Acoust. Soc. Am. **76**, 913–923 (1984).
[6]M. F. Insana, E. L. Madsen, T. J. Hall, and J. A. Zagzebski, "Tests of the accuracy of a method of data reduction for determination of acoustic backscatter coefficients," J. Acoust. Soc. Am. **79**, 1230–1236 (1986).
[7]T. J. Hall, E. L. Madsen, J. A. Zagzebski, and E. J. Boote, "Accurate depth-independent measurement of acoustic backscatter coefficients with focused transducers," J. Acoust. Soc. Am. **85**, 2410–2416 (1989).
[8]E. J. Boote, J. A. Zagzebski, E. L. Madsen, and T. J. Hall, "Instrument-independent acoustic backscatter coefficient imaging," Ultrason. Imag. **10**, 121–138 (1988).
[9]E. J. Boote, T. J. Hall, E. L. Madsen, and J. A. Zagzebski, "Improved resolution backscatter coefficient imaging," Ultrason. Imag. **13**, 347–359 (1991).
[10]C. R. Meyer, K. Fung, A. M. Aisen, M. E. Dupuy, and P. L. Carson, "Design and use of a general purpose, ergonomic, ultrasonic RF backscatter acquisition system," Ultras. Imag. **7**, 97 (1985).
[11]T. J. Hall, Ph.D. thesis, University of Wisconsin (1988).
[12]H. T. O'Neil, "Theory of focusing radiators," J. Acoust. Soc. Am. **21**, 516–526 (1949).
[13]E. L. Madsen, M. M. Goodsitt, and J. A. Zagzebski, "Continuous waves generated by focused radiators," J. Acoust. Soc. Am. **70**, 1508–1517 (1981).
[14]M. M. Goodsitt, E. L. Madsen, and J. A. Zagzebski, "Field patterns of pulsed focused transducers," J. Acoust. Soc. Am. **71**, 318–329 (1982).
[15]P. L. Carson, "Rapid evaluation of many pulse echo system characteristics by use of a triggered pulse burst generator with exponential decay," J. Clin. Ultrasound **4**, 259–263 (1976).
[16]E. L. Madsen, J. A. Zagzebski, R. A. Banjavic, and R. E. Jutila, "Tissue mimicking materials for ultrasound phantoms," Med. Phys. **5**, 391–394 (1978).
[17]E. L. Madsen, J. A. Zagzebski, M. C. MacDonald, and G. R. Frank, "Ultrasound focal lesion detectibility phantoms," Med. Phys. **18**, 1171–1180 (1991).
[18]J. A. Zagzebski, E. L. Madsen, and G. R. Frank, "A teaching phantom for ultrasonographers," J. Clin. Ultrasound **19**, 27–38 (1991).
[19]E. L. Madsen, J. A. Zagzebski, and G. R. Frank, "Oil-in-gelatin dispersions for use as ultrasonically tissue-mimicking material," Ultrasound Med. Biol. **8**, 277–287 (1982).
[20]J. J. Faran, Jr., "Sound scattering by solid cylinders and spheres," J. Acoust. Soc. Am. **23**, 405–418 (1951).
[21]S. A. Goss, R. L. Johnston, and F. Dunn, "Comprehensive compilation of empirical ultrasonic properties of mammalian tissues," J. Acoust. Soc. Am. **64**, 423 (1978).
[22]J. Ophir, T. H. Shawker, N. F. Maklad, J. G. Miller, S. W. Flax, P. A. Narayana, and J. P. Jones, "Attenuation estimation in reflection: Progress and prospects," Ultrason. Imag. **6**, 349–395 (1984).
[23]C. F. Chen, D. E. Robinson, L. S. Wilson, K. A. Griffiths, A. Manoharon, and B. D. Doust, "Clinical sound speed measurement in liver and spleen *in vivo*," Ultrason. Imag. **9**, 221–235 (1987).
[24]M. O'Donnell and H. F. Reilly, "Clinical evaluation of the B'-scan," IEEE Trans. Son. Ultrason. **SU-32**, 450 (1985).
[25]D. Nicholas, "Evaluation of backscattering coefficients for excised human tissues: Results, interpretation and associated measurements," Ultrasound Med. Biol. **8**, 17–28 (1982).